PERGAMON

International Journal of Heat and Mass Transfer 45 (2002) 2707–2718

International Journal of HEAT and MASS TRANSFER

www.elsevier.com/locate/ijhmt

Numerical modelling and experimental investigation of the fluid flow and contaminant dispersion in a channel

S. Hancu [a,1], T. Ghinda [a], L. Ma [c], D. Lesnic [b], D.B. Ingham [b,*]

[a] *The National Institute of Research and Development for Environmental Protection, Bucharest, Romania*
[b] *Department of Applied Mathematics, University of Leeds, Leeds LS2 9JT, UK*
[c] *Department of Fuel and Energy, University of Leeds, Leeds LS2 9JT, UK*

Received 26 September 2001

Abstract

This paper presents results of both a computational and a physical model of the fluid and mass transport processes in a straight channel with flow control obstructions being placed in the channel. The numerical model employs a three-dimensional CFD simulation incorporating turbulent models for the fluid and mass transport in the channel. The experimental investigations provide the necessary boundary conditions and validation data for the computational model. Large recirculating flows are observed in both the numerical and experimental investigations. Salt solutions have been used in the experimental investigations for the contaminant transport and the dispersion of the salt solution in the channel has been studied numerically. We have obtained reasonably good agreement between the numerical predictions and the experimental observations for both the fluid flow and the mass transport processes.

1. Introduction

Channel flows containing particles and contaminant materials commonly exist in various industrial and environmental engineering applications. In addition to studies where a channel has parallel vertical sides there is much interest in flows in channels which have obstructions. Therefore, it is of great interest to scientists and engineers alike to gain a better understanding of how these various obstructions may influence the fluid and mass transport in channels. A literature review shows that there has been a number of research papers on the fluid flow structure and the particle/contaminant transport in channel flows, see [1–5], which cover various aspects of contaminate laden channel flows. However, it should be noted that detailed knowledge of the flow and the contaminant dispersion in any particular group of particle laden channel flows still has to be studied through a combination of theoretical and experimental investigations [8,9]. This is largely due to the complex nature of the problem involved, leading to the experimentally obtained material dispersion coefficients varying considerably from situation to situation, see [6]. On the other hand, we are still not confident as to how we may predict from CFD simulations the fluid and mass dispersion in even the simplest of channel flows. Therefore, in addition to the study of the fluid and mass dispersion in the particular channel configurations investigated in this paper, one of the objectives of the paper is to validate the CFD models against the experimental observations in order to provide further insight into the CFD models in the predictions of the fluid and mass transport in complex channel configurations.

In this paper we present both a numerical model and experimental results for the fluid flow and mass dispersion in various partially blocked open channels. The typical layout of the channel flow studied in this paper is schematically shown in Fig. 1. The overall dimensions of the channel studied are 2 m wide and 26 m long with a typical water depth of 0.2 m. Plane blocking blades of

* Corresponding author. Tel.: +44-113-233-5113; fax: +44-113-242-9925.
E-mail address: amt6dbi@amsta.leeds.ac.uk (D.B. Ingham).
[1] Also Corresponding author.

0017-9310/02/$ - see front matter
PII: S0017-9310(02)00004-2

Nomenclature

c	contaminant concentration	x^i	Cartesian co-ordinate system
c_μ	turbulence model constant	ρ	fluid density
$c_{\varepsilon 1}$	turbulence model constant	α	turbulence model constant
$c_{\varepsilon 2}$	turbulence model constant	β	turbulence model constant
k	turbulence kinetic energy	ε	turbulence dissipation rate
p	fluid pressure	η	parameter related to the rate of strain
P	the turbulence production	δ_j^i	the Kronecker symbol
R	parameter related to the rate of strain	μ	fluid molecular viscosity
Sch	the Schmidt number	ν_t	eddy viscosity
t	time	μ_t	viscosity coefficient ($\mu_t = \rho \nu_t$)
u^i	fluid velocity	τ	Reynolds stress tensor

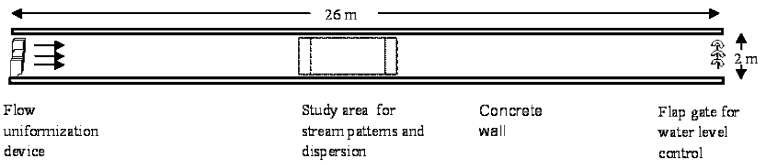

Fig. 1. A schematical diagram of the channel flow studied.

various lengths are placed in the channel perpendicular to the side walls and the bottom surface of the channel and we have studied in detail five basic configurations, see Fig. 2. Water flows into the channel passing through various successive cross-sections. The configurations of the channel flows studied in this paper are often encountered in various technical installations and environmental applications, such as in contaminant or river flow management [2,3,7].

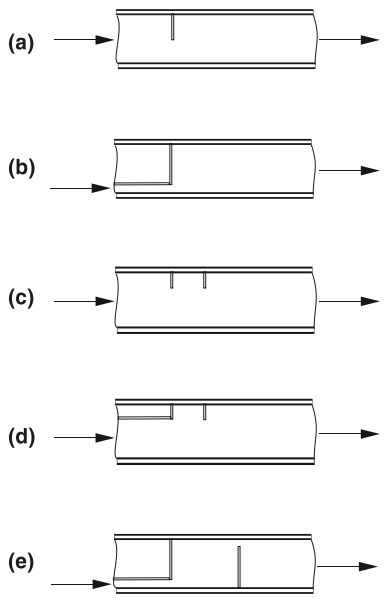

Fig. 2. Layout of the configurations formed by the blocking blades in the channel studied.

One of the main elements of the fluid flow in these configurations is the large vortex which may develop between and behind the blocking blades and this has a fundamental effect on the transport of the contaminant in the fluid flow. In order to investigate the behaviour of the contaminant dispersion in the neighbourhood of the blocking blades, the contaminant material is released into the steady flow in the upstream part of the channel. Then the variation of the contaminant concentration has been measured and modelled numerically as the contaminant passes through the blocking blades.

In the fluid flow simulations, the governing three-dimensional turbulent fluid flow equations, incorporating the RNG k–ε turbulence model, have been solved using the control volume numerical technique. The numerical modelling of the transport of the contaminant in the channel has been accomplished by numerically solving the unsteady contaminant transport equation involving the effects of the convection and diffusion of the contaminant in the water flow. The results of the numerical predictions for the fluid flow, and the variation of the contaminant concentrations, in the channel have been compared with the experimental observations.

2. Physical model

Experimental investigations have been performed in an open channel, as shown in Fig. 1, which is 26 m long

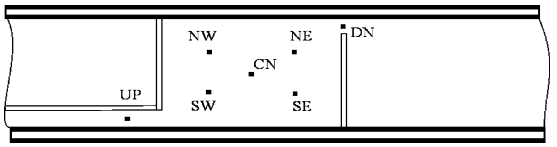

Fig. 3. The positions of the measuring devices in the experimental model.

and 2 m wide with blocking blades being placed in the channel. At the upstream end of the channel a flow control device is fitted which produces an almost constant fluid velocity across the channel. Further, a downstream flap gate has been employed in order to control the water level in the channel. Several different combinations of the blocking blades have been placed vertically from the bottom to the top of the channel, and perpendicular to the direction of the unperturbed fluid flow, to form the channel configurations as shown in Fig. 2. It should be noted that numerous other configurations have been investigated but for the purpose of this paper only those shown in Fig. 2 are discussed in detail. Finally, the channel bed and banks are smooth and flat in both the experimental and numerical investigations.

The fluid flow patterns and contaminant transport in the neighbourhood of the blocking blades have been obtained by using several visualisation techniques, such as floating papers, powders or light floats. In order to investigate the time variation of the contaminant dispersion processes, certain amounts of salt solutions have been released from an upstream location of the channel within a very small period of time, thus forming a contaminant surge at the upstream location of the channel. Then salt concentrations at seven different locations near to the blocking blades have been recorded. These seven locations are indicated in Fig. 3 and they are as follows: one measurement is taken at the location just before the upstream narrow section marked UP; one measurement is in the downstream narrow section marked DN and the remaining five measurements are located between the blocking blades, i.e. NW, NE, SW, SE and CN.

3. Numerical model

3.1. Governing equations for the fluid flow in the channel

With a typical water discharge of 0.009 m^3/s, the fluid flow in the channel is well within the turbulent flow regime ($Re \sim 10^5$) and therefore a turbulent flow model must be considered. For this high Reynolds number flow in a complex channel geometry then the Direct Numerical Simulation and the Large Eddy Simulation are numerically prohibitive and the only practical approach is to employ a turbulence model. In this study the frequently used control volume numerical technique has been employed for solving numerically the RNG k–ε turbulence model and this allows the contaminant transport simulation to be easily performed.

The flow in the complex channel studied in this paper is inherently three-dimensional, particularly in the neighbourhood of the blocking blades. A two-dimensional simulation cannot pick up the fluid flows in the third direction and this can result in a lower accuracy of the numerical predictions. Therefore, in this paper a full three-dimensional flow simulation has been employed. As far as the treatment of the free-surface is concerned, experimental results showed that the water surface elevation in the channel is extremely small and this is due to both the fairly large depth of the water and the steady nature of the fluid flow. Therefore, the water surface in this investigation has been prescribed in the numerical model according to the experimental data and it acts as a frictionless 'fix-lid' at the surface of the water flow in the numerical simulations.

The steady, incompressible fluid flow in a channel with cross-sectional variations may be mathematically described using the Navier–Stokes equations, see, for example, [10]:

$$\rho u^j \frac{\partial u^i}{\partial x^j} = -\frac{\partial p}{\partial x^i} - \frac{\partial}{\partial x^j}\left[\mu\left(\frac{\partial u^i}{\partial x^j} + \frac{\partial u^j}{\partial x^i}\right)\right] + \frac{\partial \tau^{ij}}{\partial x^j}, \tag{1}$$

$$\frac{\partial u^i}{\partial x^i} = 0, \tag{2}$$

where the superscripts $i, j = 1, 2, 3$ refer to the components in the x, y and z of the Cartesian co-ordinate system, u^i is the fluid velocity and x^i refers to the x-, y- and z-axis of the Cartesian co-ordinate system when $i = 1, 2$ and 3. Further, p, ρ and μ are the fluid pressure, density and fluid molecular viscosity, respectively, and τ^{ij} is known as the Reynolds stress tensor which represents the effects of the turbulent fluctuations on the fluid flow. Thus an appropriate turbulence model is required to link τ^{ij} with the global fluid flow parameters.

Among the numerous existing turbulence models, the k–ε model is the most frequently used turbulence model of fluid flows and it has enjoyed reasonable success in many engineering and scientific applications. However, the assumption of isotropic turbulence in the standard model often results in a large turbulent viscosity. Therefore, great effort has been devoted to developing new turbulence models, such as the much more sophisticated Reynolds Stress Models (RSMs). It appears from the literature that the RSMs are potentially superior to the standard k–ε model but the very complex formulations of the RSMs make it difficult to both implement and obtain convergence of the iterative procedure. Therefore, in all the results which are presented in this paper, the relatively newly developed ReNormalization Group (RNG) theory turbulence model has been employed

since this model has been reported to have some improvements over the standard k–ε model in the simulations of such fluid flows as is studied in this paper in which recirculating fluid flows exist, see, for example, [11].

The RNG model may be written in a form which is similar to the standard k–ε model and it relates the Reynolds stress tensor τ^{ij} to the mean fluid velocity in the following form:

$$\tau^{ij} = -\frac{2}{3}\rho k\delta^i_j + \mu_t\left(\frac{\partial u^i}{\partial x^j} + \frac{\partial u^j}{\partial x^i}\right), \tag{3}$$

where the turbulent viscosity may be expressed as a function of the turbulent kinetic energy k and its rate of dissipation ε as follows:

$$\mu_t = c_\mu \rho \frac{k^2}{\varepsilon}, \tag{4}$$

where c_μ is a constant and it has been found that the value of $c_\mu = 0.0845$, see for example, [11], gives good results for a number of investigations and therefore it has been assigned this value in all the computation presented in this paper.

For high Reynolds number fluid flows, the transport equations for k and ε in the RNG k–ε model are given by, see, for example, [11]:

Kinetic energy equation.

$$\rho u^j \frac{\partial k}{\partial x^j} = \alpha \frac{\partial}{\partial x^i}\left((\mu + \mu_t)\frac{\partial k}{\partial x^i}\right) + P - \rho\varepsilon, \tag{5}$$

where

$$P = (\mu + \mu_t)\left(\frac{\partial u^i}{\partial x^j} + \frac{\partial u^j}{\partial x^i}\right)\frac{\partial u^i}{\partial x^j} \tag{6}$$

is the term which represents the production of turbulence.

Dissipation rate equation.

$$\rho u^j \frac{\partial \varepsilon}{\partial x^j} = \alpha \frac{\partial}{\partial x^i}\left((\mu + \mu_t)\frac{\partial \varepsilon}{\partial x^i}\right) + c_{\varepsilon 1}\frac{\varepsilon}{k}P - c_{\varepsilon 2}\frac{\varepsilon}{k}\rho\varepsilon - R, \tag{7}$$

where R is a parameter which includes the rate-of-strain and it can be expressed as follows:

$$R = \rho\frac{c_\mu \eta^3(1-\eta/\eta_0)}{1+\beta\eta^3}\frac{\varepsilon^2}{k}, \quad \eta = \frac{k}{\varepsilon}\sqrt{2S_{ij}S_{ij}},$$
$$S_{ij} = \frac{1}{2}\left(\frac{\partial u^i}{\partial x^j} + \frac{\partial u^j}{\partial x^i}\right). \tag{8}$$

The values of the constants which appear in the RNG theory are usually take the values $c_\mu = 0.0845$, $c_{\varepsilon 1} = 1.42$, $c_{\varepsilon 2} = 1.68$, $\alpha = 1.3$, $\beta = 0.011$ to 0.015 and $\eta_0 = 4.38$. For more details of the RNG – k–ε turbulence model, the reader is referred to, for example, Boysan [11] and Yakhot and Orszag [12].

3.2. Governing equations for the contaminant transport in the channel

The transport of dissolved contaminants in a fluid flow typically occurs through: (i) convection, which is produced by the movement of the mean fluid flow, and (ii) diffusion, which is caused by the effect of turbulent fluctuations of the fluid flow. According to the law of mass conservation, for a control volume in a domain of the fluid flow we have the following mass-balance equation for the contaminants:

$$\frac{\partial c}{\partial t} + \frac{\partial (cu^i)}{\partial x^i} - \frac{\partial}{\partial x^i}\left(\frac{\nu_t}{Sch}\frac{\partial c}{\partial x^i}\right) = 0, \tag{9}$$

where c is the contaminant mass fraction in a computational cell and the Schmidt number Sch has been taken to be a constant value, namely 0.7, for all the numerical results presented in this paper since this is the value suggested by FLUENT [13]. Different values of Sch, say 0.6, 0.5 and even 0.2, have been examined and no significant effect has been observed on the overall results for the contaminant dispersion in the channel flows studied in this paper.

3.3. Boundary conditions and solution strategy

When solving Eqs. (1)–(9) for the fluid flow in a channel, the boundary conditions may be specified according to the operating conditions of the channel flow studied. Therefore, at the upstream boundary of the solution domain, which is located at the entrance of the channel, far upstream of the first blocking blade, a uniform downstream fluid velocity has been prescribed such that it complies with the discharge rate of the fluid flow in the channel. At the downstream boundary, which is located far downstream of the last blocking, a zero velocity gradient condition has been employed. A turbulent intensity of 5% is assumed for the inlet fluid flow since this is what is typically recommended for fluid flows in laboratory environments, see, for example, [14]. However, values of 1–10% have been considered but in all the cases considered in this paper, the results are graphically almost indistinguishable. Further, standard wall functions have been used on all the solid boundaries and a frictionless 'fixed lid' has been assumed at the water surface since the water surface elevation is almost horizontal for all the fluid flows investigated experimentally.

Subject to the above boundary conditions, the governing fluid flow equations have been numerically solved

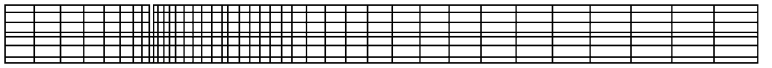

Fig. 4. A typical computational domain which has been employed in this study. It consists of $40 \times 7 \times 4$ cells in the downstream, cross and vertical directions of the channel. This represents a mesh which is four times coarser in all three directions than the finest mesh used, namely, $160 \times 28 \times 16$, which contains $160 \times 28 \times 16$ (x, y, z) cells.

using the control volume numerical method. Fig. 4 shows a plane view of a typical 3-D computational domain employed for various cases studied. The domain consists of $40 \times 7 \times 4$ cells in the downstream, cross and vertical directions of the channel and this represents a mesh which is four times coarser in all three directions than the finest mesh used, namely, $160 \times 28 \times 16$. It is observed that a relatively finer grid has been deployed in the region where the largest gradients in the fluid velocity are expected, such as the regions where large cross-sectional variations occur and near to the solid walls. Further, in order to minimise the production of artificial viscosity, the QUICK interpolation scheme has been employed for the convective terms. A grid independent test shows that the difference in the predicted fluid velocities in the channel is about 5% using the grid $160 \times 28 \times 16$ when compared with that when using the even finer grid of $320 \times 56 \times 32$.

The contaminant transport equation (9) is a typical convection–diffusion type of transport equation. Hence it may be numerically solved in the same way as that used for solving the general governing transport equations for the fluid flow, subject to the appropriate boundary conditions. However, in order to investigate the distribution of the contaminants in the channel, an unsteady solution approach has been employed when solving Eq. (9).

The general solution strategy employed is to first solve the steady fluid flow equations for the fluid flow. Having obtained solutions for the fluid flow then the unsteady contaminant transport equation (9) is solved. Since the contaminant material used in this study is a dissolved salt solution, and the concentration is very small (typically < 1 kg/m^3) then its effect on the water flow may be ignored in the numerical simulations.

4. Results and discussions

The numerical techniques discussed in Section 3 have been used in order to simulate the fluid flow and the contaminant transport throughout the various channel configurations. However, the results presented in this paper are focussed on the regions in the neighbourhood of the blocking blades in the channel, see Fig. 2, where the experimental data has been obtained. The water depth in all the experimental investigations performed was 0.2 m everywhere in the channel and this is the value we have taken in the numerical investigations.

4.1. Fluid flow patterns in the neighbourhood of the blocking blades

First let us discuss the situation when only one blocking blade is placed on one side of the channel, i.e. Configuration (a) in Fig. 2(a). Fig. 5(a) shows the numerically obtained vectors for the fluid velocity and the experimental observations in this configuration. The length of the blade is 1/2 of the channel width, i.e. the tip of the blade extends to the centre of the channel. The rate of water discharge employed is 0.009 m^3/s. It is noted in Fig. 5(a) that as the blade blocks half of the channel then it forces the fluid to go through the opening on the other side of the channel. This produces a jet type flow in the channel near the tip of the blade and this induces a large recirculating region on the downstream side of the blade in the channel. However, the recirculating velocity immediately after the blade is small in comparisons with that further downstream, as can be observed in the experimental observations shown in the right-hand side of Fig. 5(a). This may be due to the effect of the channel bank and the blocking blade which places more resistance on the recirculating flows. Further, the spread of the jet flow downstream of the blade appears to be slow.

On reducing the length of the blade from 1/2 to 1/4 of the channel width, see Fig. 5(b), the numerical predictions and experimental observations show that this reduction in the length of the blocking blade does not appear to affect the overall fluid flow pattern downstream of the blocking blade when compared with Fig. 5(a). However, the strength of the jet flow is reduced in Fig. 5(b), as one would expect due to an increase in the minimum cross-sectional area perpendicular to the fluid flow.

Fig. 5(c) shows the fluid flow when the length of the blade is 1/4 the channel width but increasing the rate of the fluid flow through the channel from 0.009 to 0.04 m^3/s. In comparison with Fig. 5(b), it is noted that on increasing the discharge rate of the fluid flow through the channel, the deflection in the direction of the fluid flow increases near to the narrowing channel blade. This also leads to an increase in the size and strength of the recirculating flow downstream of the blade but the

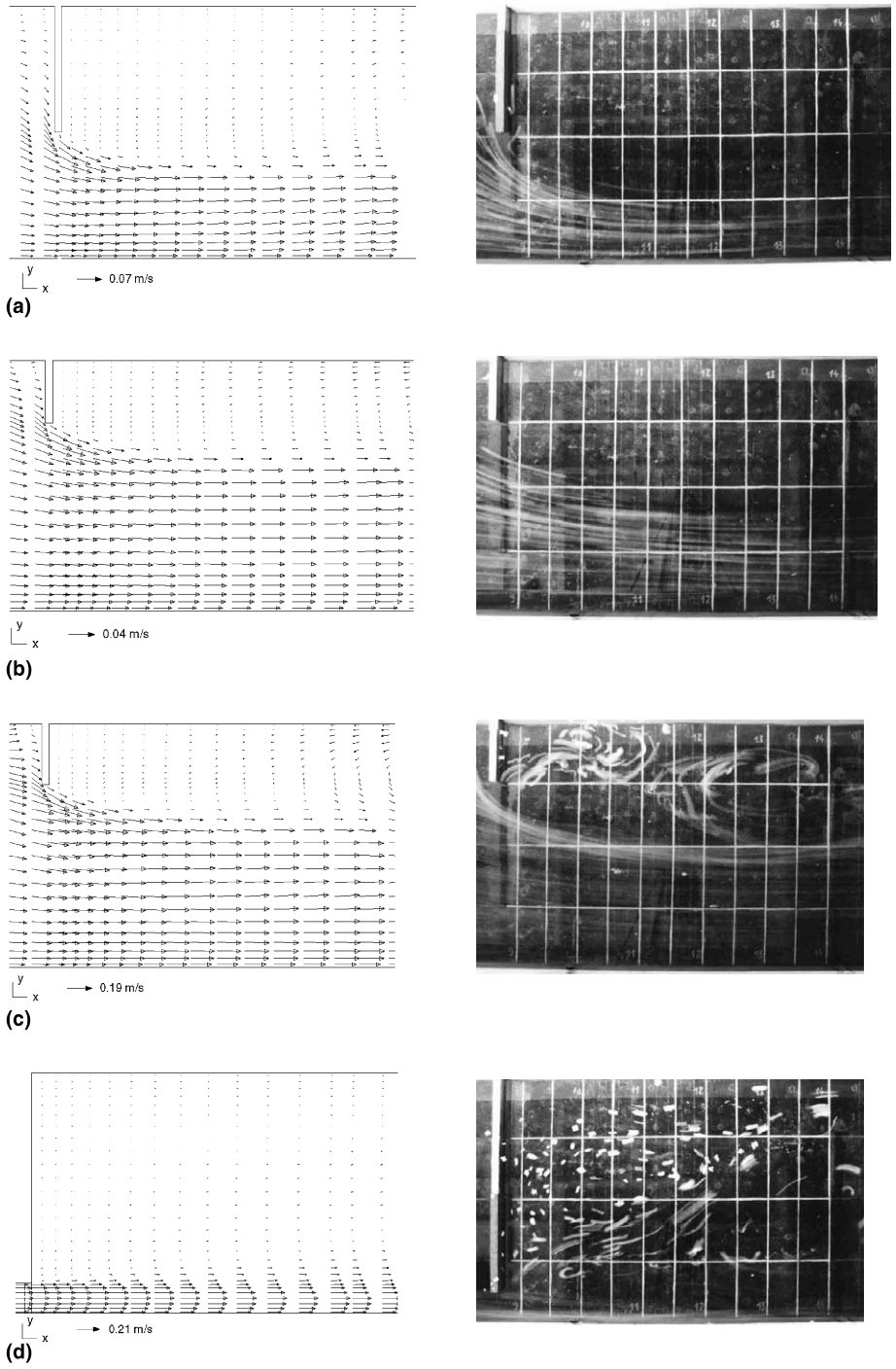

Fig. 5. Comparisons of the numerically predicted velocity vectors and the experimental observations for the fluid flows half way below the water surface in Configuration. (a) Blade length: 1/2 channel width, rate of water discharge: 0.009 m^3/s. (b) Blade length: 1/4 channel width, rate of water discharge: 0.009 m^3/s. (c) Blade length: 1/4 channel width, rate of water discharge: 0.04 m^3/s. (d) Blade length: 7/8 channel width, rate of water discharge: 0.009 m^3/s.

location of the recirculating cell in the channel is less affected.

In Configuration (b) the water flow is guided to a cross blocking blade, and this effectively forms a sudden

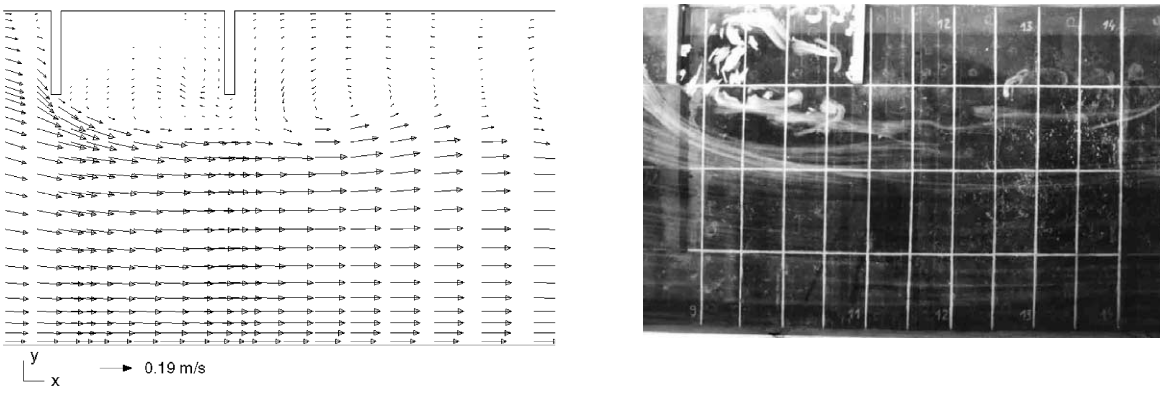

Fig. 6. Comparisons of the numerically predicted velocity vectors and the experimental observations for the fluid flows half way below the water surface in Configuration (c). The blade length is 1/4 the channel width and the rate of water discharge is 0.04 m^3/s.

opening in the channel. If the blade blocks 7/8 of the channel width and the water discharge to the channel is 0.009 m^3/s, Fig. 5(d) shows the numerical predicted flow patterns for this guided upstream fluid flow. Basically, a fluid structure which is similar to that commonly encountered in a jet flow in a sudden cross-sectional enlarged area is predicted. Now the fluid flow where there is a relatively high speed in a limited region close to the side wall of the channel is investigated. After the blade the fluid gradually mixes with the slower moving fluid in the rest of the channel and this induces large recirculations downstream of the blade.

When two blades are placed one after another on one side of the channel, see Configuration (c) in Fig. 2, then the overall fluid flow patterns change. Fig. 6 shows the numerically predicted fluid velocity vectors and the experimentally observed fluid flow in Configuration (c) when the two blades are placed parallel to each other on one side of the channel. The lengths of the blades are 1/4 of the channel width and they are spaced 1 m apart. The water discharge rate employed is 0.04 m^3/s. Fig. 6 shows that more than one recirculating fluid cell appears between and around the blades. However, due the deflecting effect that the blades have on the fluid flow, the strength of the recirculating flow, in general, between the blades is weak. This is exactly what is observed experimentally and this is also shown in Fig. 6. Further, because of the slow moving flow in the region between the blades, the recirculating fluid velocity behind the second blade is small, even when compared with the situation when just one blade is placed in the channel, see Fig. 5.

In comparison to Fig. 6, drastic changes in the fluid flow structure occurs when the flow was guided from upstream, i.e. Configuration (d). The length of the blades and the rate of water discharge are the same as for the flow in Configuration (c) shown in Fig. 6. The numerically predicted flow patterns around the blocking blades are shown in Fig. 7 and it is evident that strong

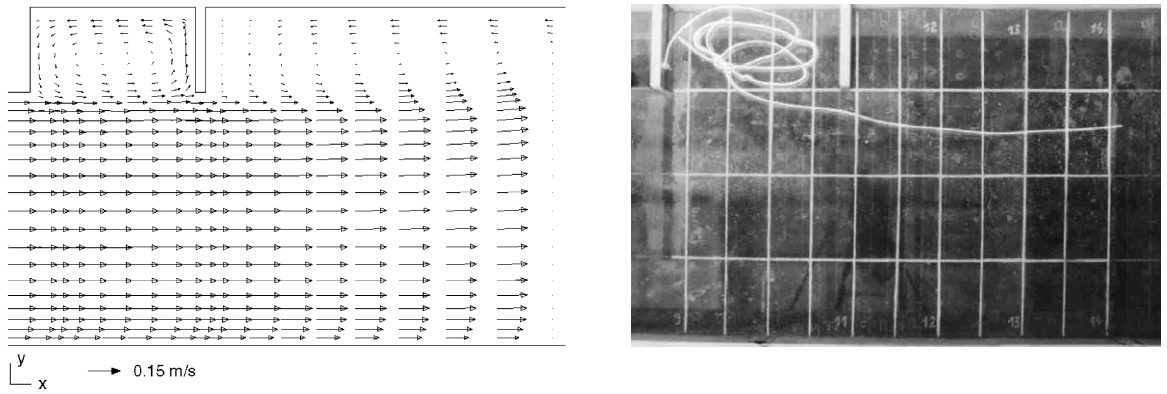

Fig. 7. Comparisons of the numerically predicted velocity vectors and the experimental observations for the fluid flows half way below the water surface in Configuration (d). The blade length is 1/4 the channel width and the rate of water discharge is 0.04 m^3/s.

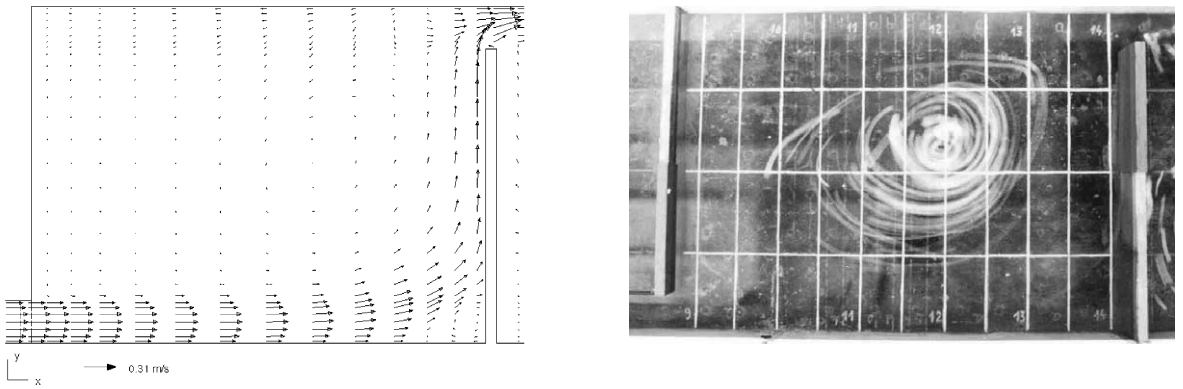

Fig. 8. Comparisons of the numerically predicted velocity vectors and the experimental observations for the fluid flows half way below the water surface in Configuration (e). The blade length is 7/8 the channel width and the rate of water discharge is 0.009 m^3/s.

recirculations are induced between the blades when the fluid flow is guided such that it passes the blades. This is exactly what is observed in the experimental results and this is also shown in Fig. 7. In addition, the two recirculating cells in Configuration (d) are not linked to one another and this contrasts to the situation in Configuration (c), see Fig. 6.

Let us now consider the situation shown in Configuration (e), see Fig. 2, when two blocking blades are placed on the opposite sides of the channel but at different locations along the channel. This forms a cell between the two blades and the side of the channel. The fluid is guided into the cells from one side of the channel and it is forced to leave the cell from a slot which is adjacent to the opposite side of the channel. Fig. 8 shows the numerically predicted fluid flow patterns in the cell half way below the water surface when the rate of water discharge employed is 0.009 m^3/s and the slots between the walls of the channel are 1/8 channel width. As can be seen in Fig. 8, a strong recirculating flow cell, which is produced by the redirection of the fluid flow by the blocking blade, dominants the fluid flow in the space between the blades. Clearly, this recirculating flow will have a strong influence on the mass dispersion through to the downstream of the channel. In addition to this large recirculating region, a small vortex is also predicted and it is located in the vicinity of the bottom-right-hand corner of the Configuration (e). These predictions are consistent with the experimental observations using floats and this is shown in the right-hand side of Fig. 8.

Further, in comparison with Configurations (a)–(d), Configuration (e) imposes the strongest resistance to the fluid flow and thus generates the strongest three-dimensional flows. This is clearly seen through the differences in the directions of the fluid flows at different

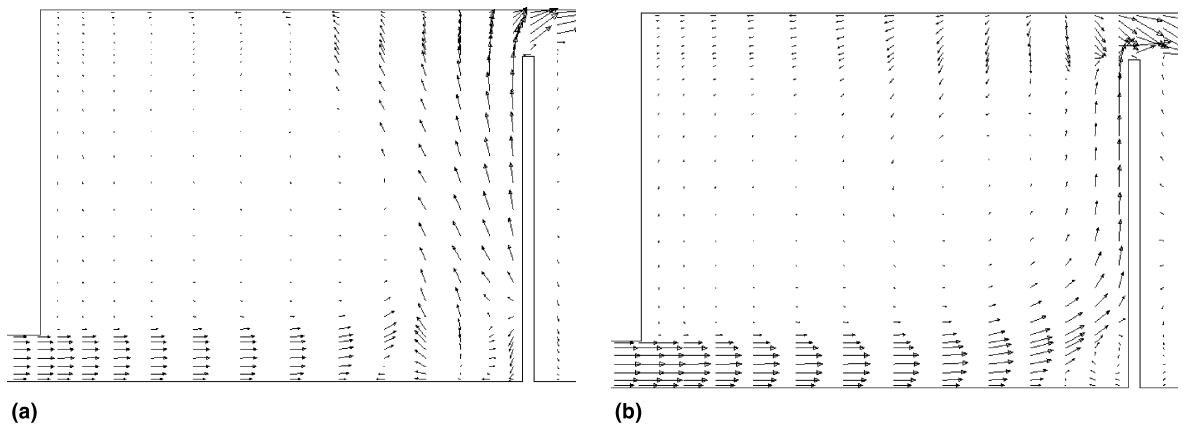

Fig. 9. Numerically predicted velocity vectors for the fluid flow near to the channel bed and near to the water surface in Configuration (e). The blade length is 7/8 the channel width and the rate of water discharge is 0.009 m^3/s.

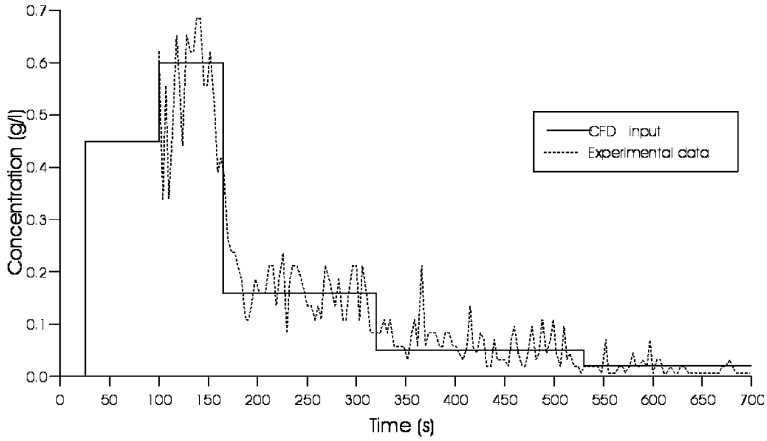

Fig. 10. Variations in the salt concentration that has been specified at the location 'UP' in Configuration (e) based on the experiment data.

depths below the water surface. At its extreme, Figs. 9(a) and (b) show the numerically predicted fluid flow patterns in the planes which are near to the channel bed and the water surface, respectively. The main fluid flow near to the bed is generally slower than it is near to the surface. However, near to the corner between the bed and the second blade, reverse currents develop where the blade forces the main fluid flow to change its direction. In addition, the vertical, z-component of the fluid flow is also observed in the vicinity of the corners between the second blade and the walls of the channel and this leads to the fluid flowing away from the walls of the channel near to these corners and these secondary flows can be observed in both Figs. 9(a) and (b).

4.2. Contaminant transports through blocking objects in the channel

In order to investigate the behaviour of the contaminant transport through the configurations such as those shown in Fig. 2, 1 kg of salt solution was released at an upstream location in the channel. The flow was guided into Configuration (e) and the consequent salt concentration in the channel has been investigated both numerically and experimentally.

In order to numerically model the changes in the salt concentrations in the channel with time, the salt concentration at the first upstream measuring location in the channel, which is marked as 'UP' in Fig. 3, is set

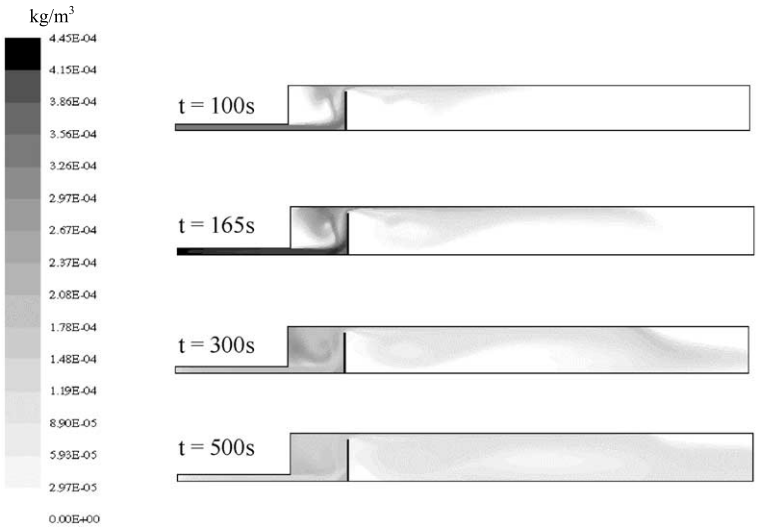

Fig. 11. Numerically predicted salt concentrations at $t = 100$, 165, 300 and 500 s after the release of the salt solution at the upstream location of the channel in Configuration (e).

according to the experimental data. Then the salt concentration in the remainder of the channel has been numerically predicted. However, since all the experimental records of the salt concentrations have been made 100 s after the release of the salt solution upstream of the channel, estimates have to be made for the salt concentrations at the location 'UP' in the time period 0–100 s. It is estimated that, according to the average fluid speed of 0.18 m/s in the guided channel, the dissolved salt would take about 25 s to reach the location 'UP' after it had been released at the upstream location in the channel. If we assume that all 1 kg of salt solution used would pass the location 'UP' within the time period from 25 to 700 s, then, with reference to the experimental data, a concentration of about 0.445 kg/m^3 would be an appropriate value at the location 'UP' for the time period of 25–100 s. Fig. 10 shows the profile of the salt concentration as a function of time which has been taken at the location 'UP' in the numerical simulations. The experimental data for the salt concentrations at the location 'UP' are shown by a dashed line in Fig. 10. The initial condition has been specified such that the salt concentration before time $t = 0$ is zero everywhere in the channel.

At the downstream boundary of the channel, which is sufficiently far from the location of the blades, a fully

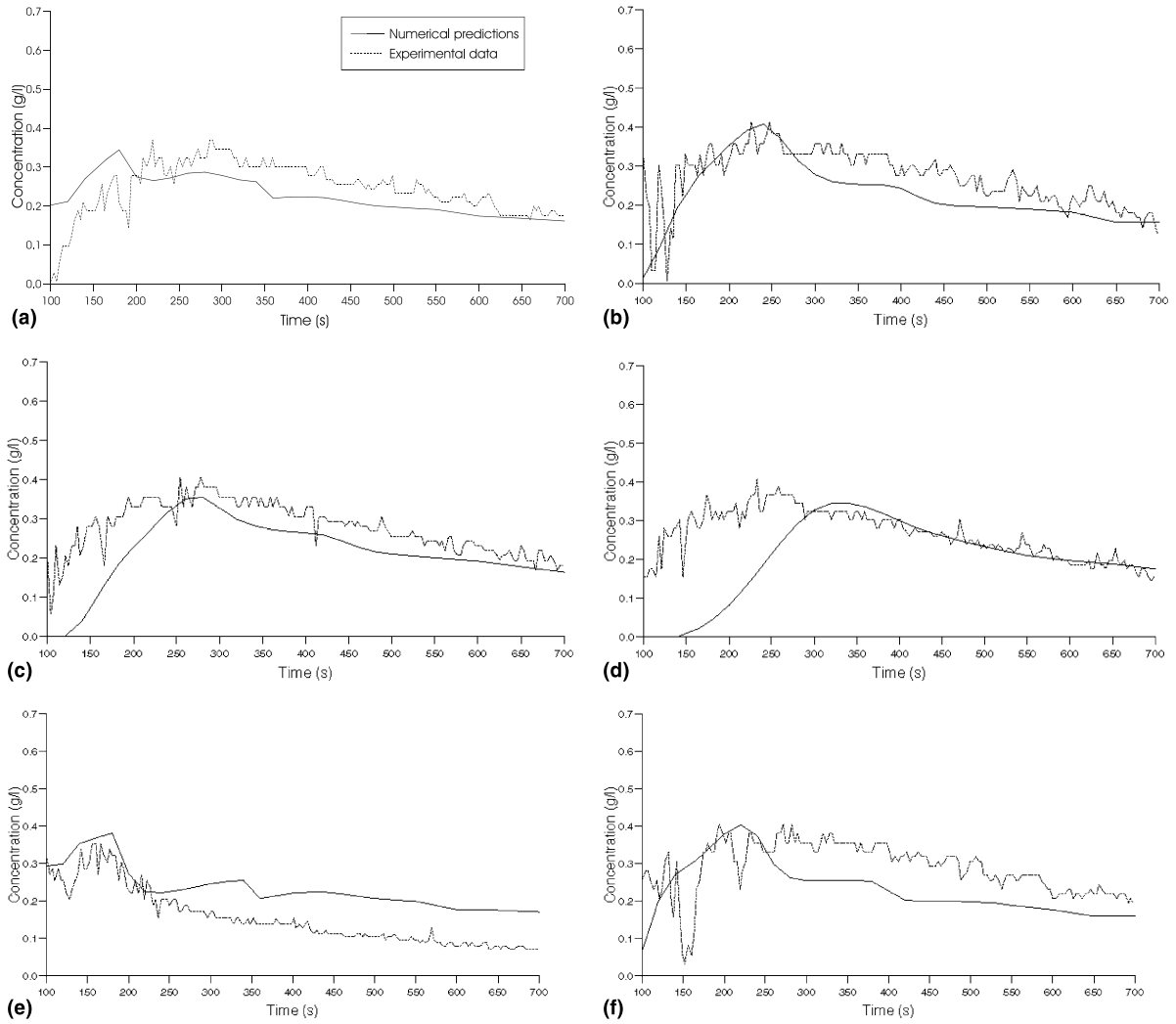

Fig. 12. Numerically predicted salt concentrations in Configuration (e) as a function of time after the release of the salt solution at the upstream location of the channel. (a) Salt concentration as a function of time at the location NE. (b) Salt concentration as a function of time at the location NW. (c) Salt concentration as a function of time at the location SE. (d) Salt concentration as a function of time at the location SW. (e) Salt concentration as a function of time at the location CN. (f) Salt concentration as a function of time at the location DN.

developed condition has been assumed such that the salt concentration is unchanged along the direction of the fluid flow. On the solid walls of the channel, the commonly employed assumption of zero normal gradient of the contaminant concentration has been employed.

Under the boundary conditions outlined above, salt concentrations across the channel have been numerically predicted using various grid sizes. It is observed that the mass concentration predictions are more sensitive to the grid size than are the fluid velocity predictions, and therefore the finer grid containing $320 \times 56 \times 32$ cells has been employed. The numerically predicted values for the mass concentration has been compared with the available experimental data.

Fig. 11 shows the numerically predicted contours for the salt concentration distribution in the channel at $t = 100$, 165, 300 and 500 s after the salt concentration at the location 'UP' has been specified according to Fig. 10. It is observed in Fig. 11 that due to the effect of the recirculating flow between the blocking blades, the contaminant is temporally confined inside the cell between the blades before it gradually is transported downstream through the small space between the blade and the side of the channel. This gives a larger residence time for the mass transfer in the cell. This could be important for some pollutants if there is a chemical reaction taking place in the fluid flow, or if the contaminant would be removed by deposition processes.

It is evident from Fig. 11 that the movement of the salt in the channel is the combined effect of both convection and diffusion processes but it is mainly through the convection of the main fluid recirculating flows. Therefore the distribution of the salt concentration also partially reflects the flow patterns in the channel where recirculating flows are clearly seen in Fig. 11.

Fig. 12 shows the variation of the salt concentration over the time interval 100–700 s at the six locations between the blocking blades where the measurements of the salt concentration have been made in the experimental investigations. These six locations are marked as SE, NE, CN, NW, SW and DN, respectively, see Fig. 3. In general, the numerical simulations are in good agreement with the experimental data for the salt concentration in the area between the blocking blades, although some discrepancies do exist, such as those shown in Figs. 12(c) and (f). However, this may well be due to the estimated boundary conditions for the salt concentration in the period of time 0–100 s at the location marked as 'UP', see Fig. 10, which has been assumed to be uniform across the channel at the inlet plane, and this does not fully reflect the history of the salt concentrations in the channel which were not recorded in the experiment. The local concentration variations are also influenced by some large fluctuations of the water flow observed during the experiments. However, under the initial and boundary conditions as shown in Fig. 10, the numerical predictions do reflect the overall variations of the dispersion processes at the six observing locations. It is seen in Fig. 12 that the salt concentration at the locations NE and DN are the first to reach their peak values and this is due to the strong convection processes which transports the salt downstream. This is followed by the locations CN, NW and SE reaching their peak values. The rise in the salt concentration at the location SE is probably a result of the diffusion processes and this causes the delay in the appearance of the peak value. After reaching their peak values, the salt concentration in the vicinity of all the six monitoring locations gradually reduces.

5. Conclusions

In this paper we have reported the combined approach of using numerical and experimental models in order to investigate the fluid flow and the contaminant transport in an open channel with various blockages being placed in the channel. The RNG turbulence model has been employed to model the turbulent flows in the channel and it is reported that this can produce more accurate numerical predictions than when using the standard k–ε model for the fluid flow past obstacles such as those presented in the channel configurations studied in this paper. The water surface has been treated as a fixed non-friction 'lid' as the experimental investigations suggest that the water surface in the channel studied is almost horizontal. The numerical model presented has successfully predicted the large recirculating fluid flows which occur in the neighbourhood of the various channel configurations studied and they are in good agreement with the experimental observations. Clearly, three-dimensional fluid flows have been observed both numerically and experimentally in terms of the directions of the fluid flows in the vicinity of the bottom and the surface. Having obtained the solution for the fluid flow, then the time-dependent contaminant transport processes in the channel have been studied. With the upstream measurement data as the time-dependent inlet boundary conditions for the numerical model, the variation of the contaminant concentrations across the channel have been obtained and these results are compared with the experimental data in the region near to the blocking blades. We have found that there is a reasonably good agreement between the numerical predictions and the experimental data for both the fluid flow and the mass transport.

In summary, in this paper it has been shown that the three-dimensional computational model of the fluid flow and mass transfer which has been employed can give reasonable predictions of both the fluid flow and mass transfer processes, both qualitatively and quantitatively for various obstructed channel flows. The CFD software which has been developed has a high potential for use in specific applications in various channel flow

configurations after further validation has been made on the model. In addition, improvements of the model are at present under consideration to include such as the turbulence model, the water surface treatment and the wall roughness.

Acknowledgements

The authors wish to thank to the British Council and the Ministry of Research in Romania and also to the boards of the institutions where they have carried out the work in favourable conditions.

References

[1] J. Shi, T.G. Thomas, J.J.R. Williams, Free-surface effects in open channel flow at moderate Froude and Reynolds numbers, J. Hydraulic Res. 38 (2000) 465–474.
[2] J.L. Rosales, A. Ortega, J.A.C. Humphrey, A numerical simulation of the convective heat transfer in confined channel flow past square cylinders: comparison of inline and offset tandem pairs, Int. J. Heat Mass Transfer 44 (2001) 587–603.
[3] K.S. Yang, Numerical investigation of instability and transition in an obstructed channel flow, AIAA J. 38 (2000) 1173–1178.
[4] N. Co, Chemical transport associated with discharge of contaminated fine particles to a steady open-channel flow, Phys. Fluids 12 (2000) 136–144.
[5] L. Ma, P.J. Ashworth, J.L. Best, D.B. Ingham, L. Elliott, L. Whitcombe, Computational fluid dynamics (CFD) and physical modelling of an upland urban river, Geomorphology (2002) (in press).
[6] J.L. Schnoor, Environmental modelling, Wiley-Interscience, New York, 1996.
[7] S. Hancu, P. Dan, A two-dimensional mathematical model for the river bed deformation, in: Proceedings of the Second International Symposium on River Sedimentation, Nanjing, China, 1983, pp. 212–218.
[8] A.J. Reynolds, Turbulent Flows in Engineering, Wiley, New York, 1974.
[9] R.H. French, Open-channel Hydraulics, McGraw-Hill Book Company, New York, 1985.
[10] G.K. Batchelor, An Introduction to Fluid Dynamics, Cambridge University Press, Cambridge, England, 2000.
[11] F. Boysan, Advanced turbulence modelling, Short Course Notes at the University of Leeds, Fluent Europe Ltd., 1995.
[12] V. Yakhot, S.A. Orszag, Renormalization group analysis of turbulence. I. Basic theory, J. Sci. Comput. 1 (1986) 1–51.
[13] FLUENT User's Guide, Volume 4, 1996, Release 4.4, Fluent Europe Ltd., Sheffield, p. 258.
[14] M. Nallasamy, Turbulence models and their applications to the prediction of internal flows – a review, Comput. Fluids 15 (1987) 151–194.